

Cavity-Assisted Manipulation of Freely Rotating Silicon Nanorods in High Vacuum

Stefan Kuhn,[†] Peter Asenbaum,[†] Alon Kosloff,[‡] Michele Sclafani,^{†,||} Benjamin A. Stickler,[§] Stefan Nimmrichter,[§] Klaus Hornberger,[§] Ori Cheshnovsky,[‡] Fernando Patolsky,[‡] and Markus Arndt^{*,†}

[†]University of Vienna, Faculty of Physics, VCQ, Boltzmanngasse 5, 1090 Vienna, Austria

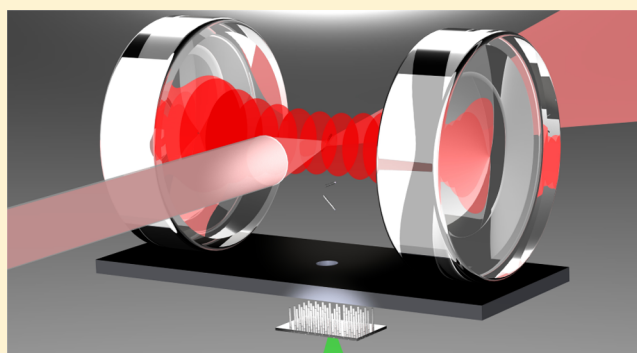
[‡]School of Chemistry, Tel-Aviv University, Ramat-Aviv 69978, Israel

[§]University of Duisburg-Essen, Lotharstraße 1, 47048 Duisburg, Germany

S Supporting Information

ABSTRACT: Optical control of nanoscale objects has recently developed into a thriving field of research with far-reaching promises for precision measurements, fundamental quantum physics and studies on single-particle thermodynamics. Here, we demonstrate the optical manipulation of silicon nanorods in high vacuum. Initially, we sculpture these particles into a silicon substrate with a tailored geometry to facilitate their launch into high vacuum by laser-induced mechanical cleavage. We manipulate and trace their center-of-mass and rotational motion through the interaction with an intense intracavity field. Our experiments show that the anisotropy of the nanorods leads to optical forces that are three times stronger than on silicon nanospheres of the same mass. The optical torque experienced by the spinning rods will enable cooling of the rotational motion and torsional optomechanics in a dissipation-free environment.

KEYWORDS: Nanoparticle launching, nanoparticle detection, silicon nanorods, cavity optomechanics



Nanoparticles often exhibit unique optical, mechanical, or electromagnetic properties because of quantum effects in confined geometries and low dimensions.¹ Complementary to that, our present study is part of a long-term effort to control the quantum properties of the objects' motion.^{2–4} First experiments demonstrating de Broglie wave optics with macromolecules⁵ were triggered by the question whether the superposition principle of quantum mechanics holds on all scales. They have led to the observation of quantum interference with masses beyond 10 000 amu.⁶ An even higher mass regime, which might give insight into the quantum-classical transition, can be reached with novel coherent manipulation schemes.⁷ Models of a spontaneous localization of the wave function,⁸ and nonstandard effects of gravity,^{9,10} will become relevant for delocalized particles in the mass range of 10⁵–10⁸ amu, and above 10¹⁰ amu, respectively. Tests of such models will require neutral, size- and shape-selected, cold, and slow nanoparticles that are mechanically isolated from their environment. This has motivated new experiments to launch and cool dielectric nanospheres in optical tweezers,^{11–13} in ion traps,¹⁴ and in free-flight.¹⁵

Here, we extend this research to rod-shaped dielectrics of tailored geometry and anisotropic polarizability. Once their rotational motion can be controlled sufficiently well, these nanorods may be suitable for realizing torsional optome-

chanics.^{16–18} Earlier experiments have shown that optomechanical torques can be exerted on nanorods in solution using the polarization or orbital angular momentum of a light field.^{19–22} The manipulation of nanoparticles in a dissipation-free environment, however, has remained challenging.²³ The coupling between rotational and motional degrees of freedom was recently demonstrated with optically trapped birefringent microspheres in a low pressure environment.²⁴

We have prepared periodic arrays consisting of more than a million silicon nanorods per square millimeter by dry-etching crystalline silicon wafers (see Methods and Materials). A scanning electron microscopy image of such an array is displayed in Figure 1A. The individual nanorods exhibit a length of 795 ± 17 nm and a diameter of 108 ± 16 nm corresponding to a mass of $(1.0 \pm 0.3) \times 10^{10}$ amu. The sample was positioned in a chamber evacuated to 10^{–6} Pa underneath an optical cavity. The backside of the sample was locally heated by a pulsed laser beam (1–3 mJ pulse energy, 6 ns duration and 532 nm wavelength) focused to 100 μ m, which desorbs the rods by laser-induced thermomechanical stress (LITHMOS).¹⁵ After launch, the freely moving and rotating rods need to pass a

Received: June 10, 2015

Revised: July 4, 2015

Published: July 13, 2015

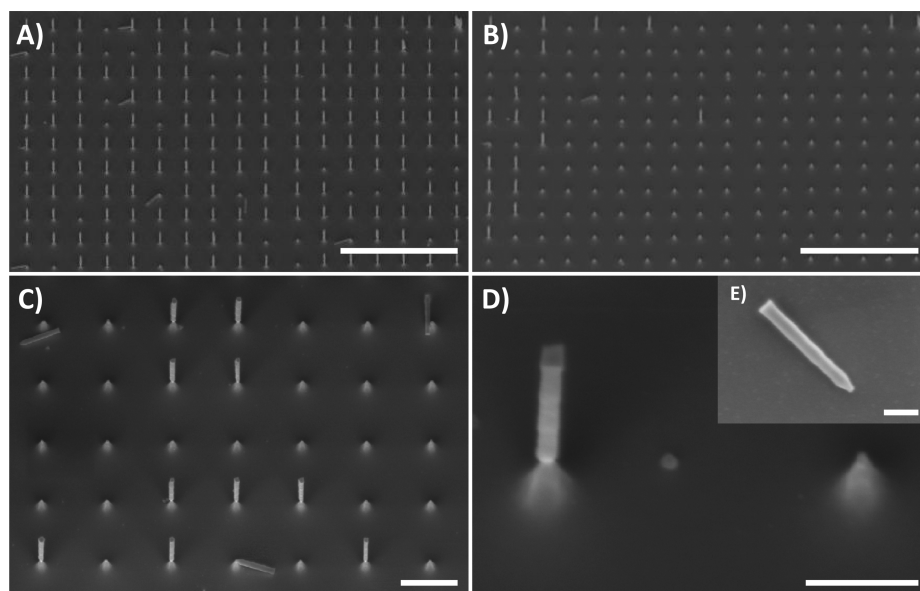


Figure 1. SEM micrographs of the nanosculptured silicon rods. Array of nanorods with underetched kerfs (A) before and (B) after LITHMOS desorption. (C and D) The kerfs define the break points where the rods crack. The actual rod length appears shortened under the oblique viewing angle. Nanorods with well-defined geometries can be launched, sent through the cavity and collected on a sample plate (E). Scale bars: (A and B) 5 μm , (C) 1 μm , (D) 400 nm, and (E) 200 nm.

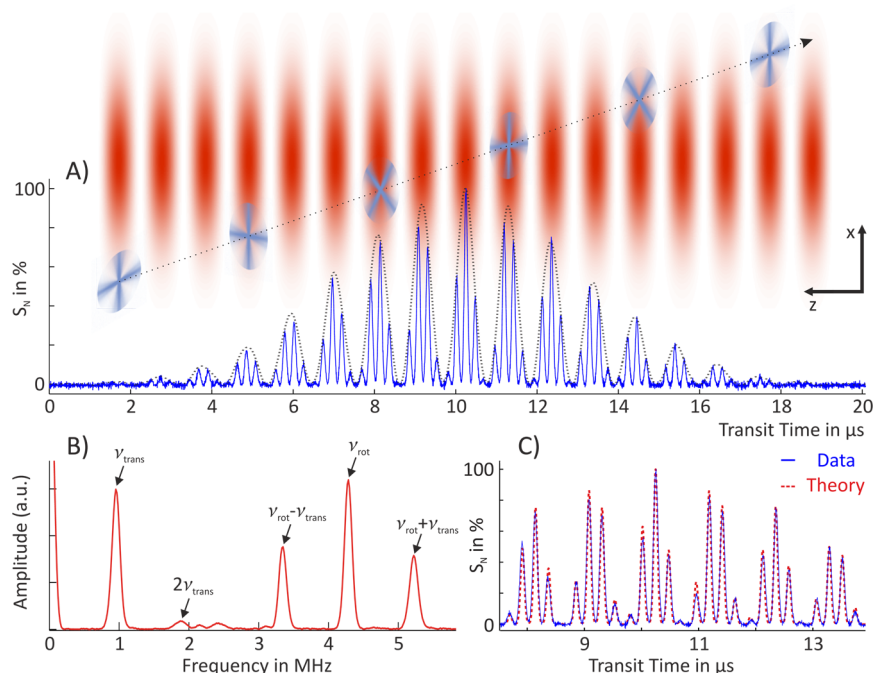


Figure 2. Tracing the nanorotor kinematics. The motion of every single nanorod can be deduced from the light it scatters while passing the cavity. (A) The signal as a function of time conveys three distinct time scales corresponding to (i) the vertical transit through the cavity mode (Gaussian envelope), (ii) the transverse motion across the standing wave (black dotted line, low frequency ν_{trans}), and (iii) the nanorod rotation (high frequency ν_{rot}). (B) These frequency contributions can also be identified in the Fourier spectrum of the signal. The particle displayed here exhibits the vertical velocity $v_x = 11.5 \pm 0.5$ m/s, the on-axis velocity $v_z = 0.77 \pm 0.05$ m/s and the rotation rate $f_{\text{rot}} = 2.15 \pm 0.03$ MHz. The geometric collimation of the incident particle trajectories permits an unambiguous distinction of the translational and rotational motion. (C) The measured scattering signal (blue solid line) is well explained by a simple theoretical model (red dashed line), see Methods and Materials and Supporting Information.

500 μm diameter and 4 mm long aperture before entering a strongly pumped high-finesse infrared cavity ($\lambda = 1560$ nm, 400 W intracavity power, 330 000 finesse, $w_0 = 65$ μm waist). The rotation rates differ from shot to shot ranging from 550 kHz up to 30 MHz; the forward velocities vary between 3 and 78 m/s.

Small kerfs etched into the nanorod base define the desired break-off conditions (see Figure 1C and D; details in the Methods and Materials). In Figure 1A and B, we show an electron micrograph of a sample spot before and after the LITHMOS pulses. It demonstrates that the rods can be

reproducibly broken off at the tailored constrictions. Figure 1E depicts a close-up of the etched conical tip of a rod after launch and recapture.

The standing light wave field of a high-finesse cavity allows us to track the translational and rotational motion of the particles. It is optically pumped by a linearly polarized, distributed-feedback laser locked close to the cavity resonance. At the laser wavelength of 1560 nm, silicon exhibits a high relative permittivity ($\epsilon_r \approx 12$) and minimal absorption. In a homogeneous field, the polarizability assumes a maximum value of $\alpha_{\parallel}/(4\pi\epsilon_0) = 6.4 \times 10^9 \text{ \AA}^3$ and a minimum value of $\alpha_{\perp}/(4\pi\epsilon_0) = 9.8 \times 10^8 \text{ \AA}^3$ when the rods are oriented parallel and perpendicular to the field, respectively.²⁵ Even for rotating rods, the polarizability averaged over all possible rotation axes, $((1/3)\alpha_{\parallel} + (2/3)\alpha_{\perp})/(4\pi\epsilon_0) = 2.8 \times 10^9 \text{ \AA}^3$, is larger than for a silicon nanosphere of the same mass, $\alpha_{\text{sph}}/(4\pi\epsilon_0) = 1.4 \times 10^9 \text{ \AA}^3$.

We can trace each nanorotor using the light it scatters into the direction perpendicular to both the cavity axis and the field polarization. We collect this light in a 1 mm multimode fiber placed at a distance of 200 μm from the cavity center. The detected intensity depends on the rod's position in the standing wave and also on its orientation (see Methods and Materials).

When a symmetric rotor enters the cavity and moves freely along the cavity axis, we expect a modulation of the scattering signal at two distinct frequencies: One is the translational frequency $\nu_{\text{trans}} = 2\nu_z/\lambda$ of the particle passing the standing-wave nodes with velocity ν_z , the second one is twice the rotation frequency, $\nu_{\text{rot}} = 2f_{\text{rot}}$.

Figure 2A displays the normalized scattering intensity of a freely rotating nanorod, $S_N \equiv (I_s/I_c)/\max(I_s/I_c)$, where I_s is the measured scattering signal and I_c the simultaneously recorded intracavity intensity. Panel C shows that it agrees well with the theoretical expectations for light scattering at dielectric needles (red dotted line). An expression for the expected scattering signal as a function of the rod's center-of-mass position and orientation is presented in the Methods and Materials. This signal is evaluated along the rotor trajectory. In the Supporting Information, we provide a full comparison between the measured signal in panel A and the model, simulating the trajectory with an appropriate choice of the initial conditions and the field amplitude. The corresponding Fourier spectrum, depicted in panel B, exhibits the distinct frequency contributions of translation and rotation.

For slow rods, we could observe cavity-induced translational channelling, that is, one-dimensional trapping along an antinode of the standing light wave. One such case is displayed in Figure 3, where the scattering signal (panel A) differs significantly from Figure 2. By low-pass filtering the scattering signal, we can eliminate the modulation due to the rotation of the rod. The resulting modulation envelope (black dotted curve) does not drop to zero while the particle is close to the center of the Gaussian beam. During this time the frequency related to the transverse motion of the rod is influenced significantly. In panel B, we reconstruct the particle trajectory through the cavity mode from the time evolution of the light scattering curve.¹⁵ This is reproduced in a simulation of the rod's motion under the influence of the cavity field (see Supporting Information Figure S2).

The optical channelling effect benefits from the geometrically enhanced induced dipole moment, due to the strong anisotropy of the rods.²⁵ For silicon nanorods rotating in the plane perpendicular to the cavity axis the orientation-averaged

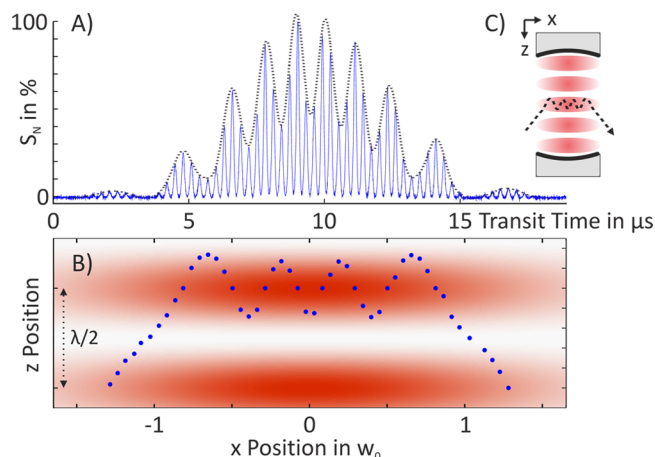


Figure 3. Transverse optical forces. (A) Scattering signal of a spinning nanorod temporarily channelled in the standing-wave field. As the particle approaches the center of the cavity mode along x , after approximately 5 μs , the optical potential of the standing light wave is sufficiently deep to trap the rod's center of mass resulting in an oscillatory motion around an antinode along z . Thus, the modulation envelope (black dotted line) no longer falls to zero, in contrast to Figure 2 (panel A, black dotted line). The oscillation frequency of up to 470 kHz is deduced from the separation between the envelope peaks. A silicon sphere with the same volume would only be trapped at a frequency of 290 kHz.¹⁵ The fast modulation of the scattered light (blue solid line) is due to the rotation of the rod at $f_{\text{rot}} = 1.7 \text{ MHz}$. (B) Reconstruction of the trajectory of the rod. (C) Illustration of the experimental geometry.

polarizability in the light field, $(\alpha_{\parallel} + \alpha_{\perp})/2$, is enhanced by a factor of 2.7 in comparison to silicon spheres of the same mass. In Figure 3, we observe an enhancement of the trapping potential by a factor of 2.6.

In addition to the optical force on the particle's center of mass, the cavity field exerts a torque on the rods, which tends to align them along the field polarization axis.²⁶ Figure 4 displays the scattering curve of a slowly rotating nanorod manipulated in both its center-of-mass motion and its rotation. In analogy to Figure 3, we observe transverse channelling, but the rotation rate (black circles) is now influenced significantly by the optical torque. The influence of the optical potential on the rotation rate is most pronounced at around 12 μs . The net increase of rotational energy during the transit of the rod can be attributed to the coupling between the rotational degrees of freedom and the time dependent optical potential (see Supporting Information Figure S3).

In conclusion, we have presented a method to tailor, launch, track, and manipulate high-mass silicon nanorods with well-defined geometry and high aspect ratio. Light scattering inside a high-finesse infrared cavity allows us to follow the translational and rotational motion of the nanorotors in real time. For some of the rods, cavity assisted 1d-trapping and even rotational forces could be demonstrated. Our results are in good agreement with theoretical expectations and show that the rod-like shape enhances the interaction between the particles and the cavity field significantly, compared to silicon nanospheres of the same mass. Optomechanical trapping and cooling of the center-of-mass motion^{4,11–15} will benefit from aligning the rods along the axis of polarization. Recent studies on single particle thermodynamics^{27–29} may be extended to rotating systems. Our results represent a first step toward realizing rotational and torsional nano-optomechanics^{16–18,30,31}

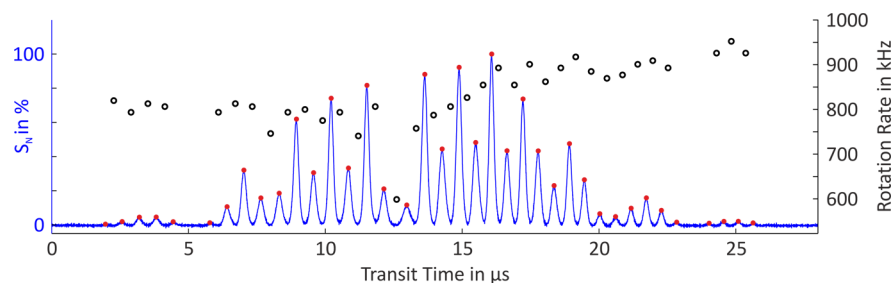


Figure 4. Optically induced torque. Scattering signal (blue curve) of a channelled nanorod, whose average rotation rate (black circles, right scale) is deduced from the separation of two adjacent scattering maxima (red dots), that is, half a rotation period. We observe that the particle first spins down to 600 kHz before it speeds up again to beyond 900 kHz (see also Supporting Information Figure S3).

and rotational cooling, which may become applicable to delicate biological nanomaterials such as the similarly shaped tobacco mosaic virus.^{32,33}

Methods and Materials. Nanorod Sculpting. The silicon nanorod arrays were fabricated from a single crystalline Si wafer by adapting a previously described dry etching method.³⁴ The 380 μm thick, $\langle 100 \rangle$ cut and p-doped wafers exhibit a resistivity of 1–10 $\Omega\text{ cm}$. They were cleaned by sonication, first in acetone then in isopropyl alcohol (IPA), each for 5 min. They were then thoroughly rinsed with deionized water and dried in a stream of N_2 . The clean Si wafers were spin coated with MMA resist (Copolymer resist EL9, MicroChem) at 4000 rpm for 60 s, followed by baking at 180 $^\circ\text{C}$ on a hot plate for 2 min. PMMA resist (Polymer resist A2, MicroChem) was deposited on the MMA layer by spinning at 2000 rpm for 60 s, followed by baking at 180 $^\circ\text{C}$ on a hot plate for 2 min.

An array of 250 nm diameter circular dots with 1 μm spacing was written using a Raith 150 ultrahigh-resolution e-beam lithography system (Raith GmbH, Dortmund, Germany). The patterned wafer was developed in MIBK/IPA 1:3 for 1 min, followed by rinsing with IPA for 20 s and drying in an N_2 stream. A nickel dot array was prepared by e-beam evaporating a 100 nm thick nickel layer at a base pressure of 10^{-7} Torr with a rate of 1 $\text{\AA}/\text{s}$. Finally, the remaining resist was lifted-off in an acetone/IPA 1:1 solution, washed with IPA, and dried. The nickel nanodot arrays served as masks in the following dry etching.

Vertical silicon nanowire arrays were fabricated by applying time-multiplexed reactive ion etching in an inductively coupled plasma deep reactive ion etching machine (ICP-DRIE, PlasmaTherm SLR 770). In order to form nanopillars with a well-defined breaking point, we have implemented a Bosch process, that is, passivation followed by anisotropic etching. A variation of the ratio between the etching and the passivation times varies the scalloping and leads to different rod diameters. On the basis of this, we set up a three-stage etching process: six “passivation-etching” sequences with a time ratio of 1:1 allowed us to form 700 nm long nanorod segments. In order to create the breaking points, the ratio of the time windows was logarithmically changed to 0.7:1 during four further steps. Finally, a wider base was formed by changing the interval ratio linearly to 2:1 in six further steps. The silicon rods were cleaned by removing the nickel caps chemically.

Scattering Theory. In order to compute the normalized scattered light intensity S_N , the rods are modeled as thin, homogeneous, dielectric needles of length L , diameter D , and relative permittivity ϵ_r . We adopt the scattering theory for dielectric needles,³⁵ valid in the limit $L \gg D/2$ and $(\sqrt{\epsilon_r}kD)/2 \ll 1$, to a standing-wave situation. The light

intensity in the direction perpendicular to both the cavity axis \mathbf{e}_z and the field polarization axis \mathbf{e}_x is then proportional to

$$\frac{I_S}{I_C} \propto k^4 D^4 L^2 \left(\frac{\epsilon_r - 1}{\epsilon_r + 1} \right)^2 |\mathbf{e}_y \times \mathbf{u}_{\text{int}}|^2 \times [S_+^2 + 2 \cos(2kz) S_+ S_- + S_-^2] e^{-2(x^2 + y^2)/w_0^2}$$

with $k = 2\pi/\lambda$ the wavenumber, w_0 the cavity waist, and $S_{\pm} = \text{sinc}[\mathbf{n} \cdot (\mathbf{e}_z \pm \mathbf{e}_y)kL/2]$. Here, we denote the center-of-mass position of the rod by (x, y, z) , and the orientation of the rod is determined by the radial unit vector \mathbf{n} . The internal field points in the direction $\mathbf{u}_{\text{int}} = 2\mathbf{e}_x + (\epsilon_r - 1)(\mathbf{n} \cdot \mathbf{e}_x)\mathbf{n}$.

For comparison with the experiment in Figure 2C and in Supporting Information Figure S1, the scattering intensity is evaluated along the rotor trajectory and normalized with respect to its maximum. The simplified equations of motion (given in the Supporting Information) reproduce the experimental observation remarkably well, although we have $(\sqrt{\epsilon_r}kD)/2 \simeq 0.7$. A precise description of the optical forces and torques requires advanced (numerical) techniques.³⁶

■ ASSOCIATED CONTENT

● Supporting Information

We provide simulations of the rod's dynamics for the experimental results displayed in Figures 2–4. The Supporting Information is available free of charge on the ACS Publications website at DOI: 10.1021/acs.nanolett.5b02302.

■ AUTHOR INFORMATION

Corresponding Author

*E-mail: markus.arndt@univie.ac.at.

Present Address

[†]Institut de Ciències Fotoniques, 08860 Castelldefels, Barcelona, Spain.

Notes

The authors declare no competing financial interest.

■ ACKNOWLEDGMENTS

Our work has been supported by the European Commission (304886) as well as by the Austrian Science Fund (FWF): W1210-3 and P27297. We acknowledge support by S. Puchegger and the faculty center for nanostructure research at the University of Vienna in imaging the nanorods. F.P. acknowledges the Legacy Program (Israel Science Foundation) for its support.

■ REFERENCES

- (1) Krahne, R.; Manna, L.; Morello, G.; Figuerola, A.; George, C.; Deka, S. *Physical Properties of Nanorods*; Springer: Berlin, 2013.
- (2) Hornberger, K.; Gerlich, S.; Haslinger, P.; Nimmrichter, S.; Arndt, M. *Rev. Mod. Phys.* **2012**, *84*, 157–173.
- (3) Arndt, M.; Hornberger, K. *Nat. Phys.* **2014**, *10*, 271–277.
- (4) Bateman, J.; Nimmrichter, S.; Hornberger, K.; Ulbricht, H. *Nat. Commun.* **2014**, *5*, 4788.
- (5) Arndt, M.; Nairz, O.; Vos-Andreae, J.; Keller, C.; van der Zouw, G.; Zeilinger, A. *Nature* **1999**, *401*, 680–682.
- (6) Eibenberger, S.; Gerlich, S.; Arndt, M.; Mayor, M.; Tuxen, J. *Phys. Chem. Chem. Phys.* **2013**, *15*, 14696–14700.
- (7) Haslinger, P.; Dörre, N.; Geyer, P.; Rodewald, J.; Nimmrichter, S.; Arndt, M. *Nat. Phys.* **2013**, *9*, 144–148.
- (8) Bassi, A.; Lochan, K.; Satin, S.; Singh, T. P.; Ulbricht, H. *Rev. Mod. Phys.* **2013**, *85*, 471–527.
- (9) Diosi, L. *Phys. Lett. A* **1987**, *120*, 377–381.
- (10) Penrose, R. *Gen. Rel. Grav.* **1996**, *28*, 581–600.
- (11) Li, T.; Kheifets, S.; Raizen, M. G. *Nat. Phys.* **2011**, *7*, 527–530.
- (12) Gieseler, J.; Deutsch, B.; Quidant, R.; Novotny, L. *Phys. Rev. Lett.* **2012**, *109*, 103603.
- (13) Kiesel, N.; Blaser, F.; Delic, U.; Grass, D.; Kaltenbaek, R.; Aspelmeyer, M. *Proc. Natl. Acad. Sci. U. S. A.* **2013**, *110*, 14180–14185.
- (14) Millen, J.; Fonseca, P. Z. G.; Mavrogordatos, T.; Monteiro, T. S.; Barker, P. F. *Phys. Rev. Lett.* **2015**, *114*, 123602.
- (15) Asenbaum, P.; Kuhn, S.; Nimmrichter, S.; Sezer, U.; Arndt, M. *Nat. Commun.* **2013**, *4*, 2743.
- (16) Shi, H.; Bhattacharya, M. *J. Mod. Opt.* **2013**, *60*, 382–386.
- (17) Yin, Z.; Geraci, A.; Li, T. *Int. J. Mod. Phys. B* **2013**, *27*, 1330018.
- (18) Müller, T.; Reinhardt, C.; Sankey, J. C. *Phys. Rev. A: At., Mol., Opt. Phys.* **2015**, *91*, 053849.
- (19) Bonin, K. D.; Kourmanov, B. *Opt. Express* **2002**, *10*, 984–989.
- (20) Paterson, L.; MacDonald, M. P.; Arlt, J.; Sibbett, W.; Bryant, P. E.; Dholakia, K. *Science* **2001**, *292*, 912–914.
- (21) Jones, P. H.; Palmisano, F.; Bonaccorso, F.; Gucciardi, P. G.; Calogero, G.; Ferrari, A. C.; Marago, O. M. *ACS Nano* **2009**, *3*, 3077–3084.
- (22) Tong, L.; Miljkovic, V. D.; Kall, M. *Nano Lett.* **2010**, *10*, 268–73.
- (23) Marago, O. M.; Jones, P. H.; Gucciardi, P. G.; Volpe, G.; Ferrari, A. C. *Nat. Nanotechnol.* **2013**, *8*, 807–19.
- (24) Arita, Y.; Mazilu, M.; Dholakia, K. *Nat. Commun.* **2013**, *4*, 2374.
- (25) Van De Hulst, H. C. *Light scattering by small particles*; Wiley: New York, 1957.
- (26) Bishop, A. I.; Nieminen, T. A.; Heckenberg, N. R.; Rubinsztein-Dunlop, H. *Phys. Rev. A: At., Mol., Opt. Phys.* **2003**, *68*, 033802.
- (27) Gieseler, J.; Novotny, L.; Quidant, R. *Nat. Phys.* **2013**, *9*, 806–810.
- (28) Gieseler, J.; Quidant, R.; Dellago, C.; Novotny, L. *Nat. Nanotechnol.* **2014**, *9*, 358–64.
- (29) Millen, J.; Deesuwana, T.; Barker, P.; Anders, J. *Nat. Nanotechnol.* **2014**, *9*, 425–429.
- (30) Rubin, J. T.; Deych, L. I. *Phys. Rev. A: At., Mol., Opt. Phys.* **2011**, *84*, 023844.
- (31) Bhattacharya, M. *J. Opt. Soc. Am. B* **2015**, *32*, B55–B60.
- (32) Ashkin, A.; Dziedzic, J. M. *Science* **1987**, *235*, 1517–1520.
- (33) Romero-Isart, O.; Juan, M.; Quidant, R.; Cirac, J. *New J. Phys.* **2010**, *12*, 033015.
- (34) Pevzner, A.; Engel, Y.; Elnathan, R.; Ducobni, T.; Ben-Ishai, M.; Reddy, K.; Shpaisman, N.; Tsukernik, A.; Oksman, M.; Patolsky, F. *Nano Lett.* **2010**, *10*, 1202–1208.
- (35) Schiffer, R.; Thielheim, K. *J. Appl. Phys.* **1979**, *50*, 2476–2483.
- (36) Simpson, S. H. *J. Quant. Spectrosc. Radiat. Transfer* **2014**, *146*, 81–99.